

# Electro-optical modulation of light polarization in a nonlocal lithium niobate metasurface

Agostino Di Francescantonio,<sup>1, a)</sup> Alessandra Sabatti,<sup>2</sup> Eleni Prountzou,<sup>2</sup> Maria Antonietta Vincenti,<sup>3</sup> Luca Carletti,<sup>3</sup> Attilio Zilli,<sup>1</sup> Michele Celebrano,<sup>1</sup> Rachel Grange,<sup>2</sup> and Marco Finazzi<sup>1</sup>

<sup>1)</sup>*Politecnico di Milano, Physics Department, Milano, Italy.*

<sup>2)</sup>*ETH Zürich, Department of Physics, Institute for Quantum Electronics, Optical Nanomaterial Group, Zürich, Switzerland.*

<sup>3)</sup>*Università di Brescia, Department of Information Engineering, Brescia, Italy.*

We report the experimental realization of a LiNbO<sub>3</sub> metasurface for electro-optic modulation of light polarization in the telecommunication band. High- $Q$  quasi-bound states in the continuum are employed to enhance the modulation of amplitude and phase of an impinging beam by a driving electric field, leading to efficient polarization rotation and conversion. We quantified modulation effects under a CMOS-compatible bias at 1 MHz frequency, achieving a variations of 5% in the Stokes parameters and a variation of the polarization ellipse angles of about 3° for the transmitted light. These results demonstrate that dynamic polarization and phase modulation can be attained in a compact platform, highlighting the potential of high- $Q$  resonant LiNbO<sub>3</sub> metasurfaces for enhanced light–matter interaction in subwavelength electro-optic devices.

---

<sup>a)</sup>Also at EPFL, Institute of Mechanical Engineering, Laboratory of Nanoscience for Energy Technologies, Lausanne, Switzerland.

## I. INTRODUCTION

Optical metasurfaces – artificial arrangements of nanostructures of sub-wavelength thickness – provide a versatile platform for tailoring light-matter interaction and manipulate the wavefront of propagating optical beams<sup>1</sup>.

In particular, metasurfaces enable precise control over the polarization state of light, which can be achieved by tailoring the phase and amplitude of the electromagnetic field<sup>2</sup> or by exploiting nonlinear light-matter interactions<sup>3</sup>. A wide variety of metasurface-based polarization devices have been reported in the literature<sup>4</sup>, exhibiting advanced functionalities ranging from polarization conversion<sup>5</sup> and metalensing<sup>6</sup> to imaging<sup>7</sup>, nonlinear generation of circularly polarized light<sup>8</sup>, and Bell states engineering<sup>9</sup>, to name a few.

The reconfiguration of metasurfaces properties by means of external stimuli<sup>10</sup> – typically thermal<sup>11</sup>, electrical<sup>12</sup> or optical<sup>13</sup> – is receiving a rapidly-growing interest. In particular, achieving active control of a metasurface polarization response represents a crucial step toward the realization of devices capable of on-demand polarization control and modulation.

Materials exhibiting a tunable birefringence are commonly employed to dynamically control the phase of a linearly-polarized optical wave in commercial phase and polarization modulators. These devices commonly rely on phase transitions in liquid crystals, photoelastic effects or the linear electro-optic (EO), also named Pockels' effect, which are typically actuated by an electric signal. The applied bias yields a change in the material refractive index,  $\Delta n$ , which translates into a dephasing  $\Delta\delta = 2\pi\Delta nl/\lambda$  introduced over a propagation length  $l$  inside the medium. Among the mentioned mechanisms for electrical modulation, the EO effect arising from a nonlinear interaction between a low-frequency electric field  $\mathbf{E}_{\text{EO}}$  and an optical field, produces a change in the  $i$ -th component of the refractive index tensor  $\Delta n_i = -\frac{1}{2}n^3 r_{ij} E_{\text{EO},j}$ , where  $r_{ij}$  is an element of the material EO tensor. The main advantages of the EO effect reside in the high modulation frequencies that can be achieved, potentially extending above hundreds of GHz<sup>14</sup>, and in the absence of Joule dissipation, making it an ideal mechanism for high-speed, energy-efficient on-chip operations. However, the limited refractive index change  $\Delta n$  achievable in routinely employed EO materials – where the largest value of the coefficients  $r_{ij}$  are typically smaller than  $100 \text{ pm V}^{-1}$  – imposes relatively large propagation lengths  $l \gg \lambda$  (often in the millimeter range) and strong applied bias to obtain a sizable phase shift  $\Delta\delta$  in EO devices.

Optical metasurfaces offer a route to overcome such a constraint by exploiting the large field

confinements and enhancements associated with photonic resonances. By trapping light in the nanostructure,  $\Delta\delta$  is boosted by the resonance quality-factor  $Q$ , achieving sizeable values even in sub-wavelength thickness samples. State-of-the-art EO metasurfaces are designed to maximize the modulation efficiency leveraging nonlocal, high- $Q$  resonant modes, like guided-mode resonances and quasi-bound-states in the continuum (quasi-BICs), boosting nonlinear light-matter interaction at the nanoscale<sup>15</sup>. We point out that remarkably large  $Q$  ( $> 10^4$ ), customarily achieved in silicon integrated photonic devices (e.g. micro-ring resonators, microcavities and 2D photonic crystal<sup>16–18</sup>), can result impractical in optical metasurfaces, where the interrogation and manipulation of propagating light is crucial. Yet, the realization of even moderate  $Q$  values ( $10^3 – 10^4$ ) is often elusive in materials with large electro-optic coefficients, such as lithium niobate ( $\text{LiNbO}_3$ ), due to fabrication constraints. Significant advancements in micro- and nanofabrication techniques recently enabled the realization of optical devices characterized by a remarkable quality, allowing the realization of resonances with ever increasing  $Q$  values. In this frame, EO devices based on  $\text{LiNbO}_3$ <sup>19,20</sup>, and organic polymers<sup>21</sup>, have demonstrated a steady performance improvement over the last few years, culminating in intensity modulation efficiencies exceeding  $1 \times 10^{-2} \text{ V}^{-1}$  and modulation frequencies in the GHz range<sup>22–26</sup>, which represent important milestones in the development of EO metasurfaces.

The use of the EO effect to control light polarization in optical metasurfaces has only been suggested by few theoretical studies<sup>27–29</sup> while the experimental demonstration of light polarization modulation has only been achieved in nanoscale devices employing other reconfiguration mechanisms<sup>30–32</sup>.

In this letter we bridge this gap presenting a  $\text{LiNbO}_3$  EO metasurface that modulates the polarization of a transmitted beam in the telecommunication band. The device is based on a design that already demonstrated<sup>23</sup> an intensity modulation efficiency of  $1.5 \times 10^{-2} \text{ V}^{-1}$  over a band of about 1 GHz and a second-harmonic generation modulation of  $1.2 \times 10^{-1} \text{ V}^{-1}$ . Here we show that the same architecture can exploit polarization-sensitive nonlocal resonances to modulate the phase retardation of one specific linear polarization with respect to the perpendicular one by about 0.05 rad. We thus provide the first experimental demonstration of a fast EO metasurface that changes the rotation angle and ellipticity of the incoming polarization by  $\pm 3^\circ$  with applied bias of  $\pm 5 \text{ V}$ .

## II. RESULTS

Figure 1a provides a schematic of a  $\text{LiNbO}_3$  metasurface modulating the light polarization by means of the electro-optic effect. An  $x$ -cut  $\text{LiNbO}_3$  thin film on top of an insulating  $\text{SiO}_2$  layer is patterned with asymmetric nanowires, aligned parallel to the  $\text{LiNbO}_3$  crystallographic  $z$  axis, to form a one-dimensional periodic grating with in-plane broken symmetry. The optical field imping-

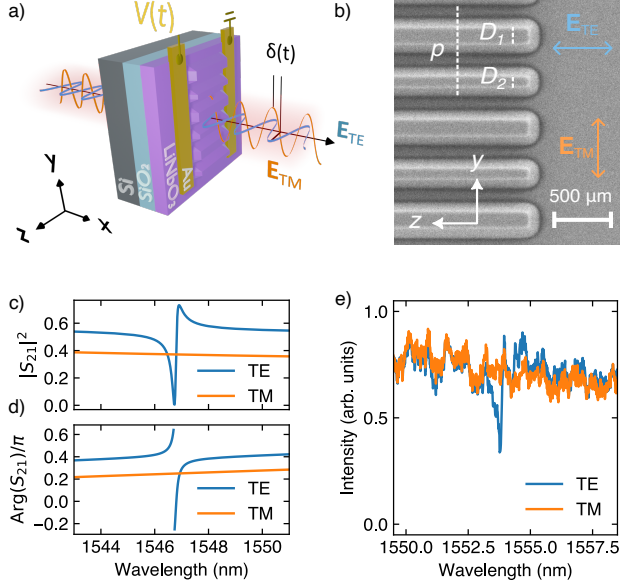


FIG. 1. **a)** Illustration of a polarization modulator made by an  $x$ -cut lithium niobate ( $\text{LiNbO}_3$ ) on insulator grating. Any mixed polarization state (e.g., an input beam polarized at  $45^\circ$  with respect to both the  $x$  and  $y$  axes) is dynamically tuned by an external bias  $V(t)$ , which modifies the relative phase  $\delta(t) = \delta_{\text{TE}}(t) - \delta_{\text{TM}}$  between the transverse electric (TE) and magnetic (TM) components (blue and orange, respectively) of the electric field via the electro-optic effect. **b)** SEM micrograph of the investigated  $\text{LiNbO}_3$  grating, with out-of-plane crystallographic  $x$ -axis, periodicity  $p = 800\text{ nm}$ , and asymmetry  $(D_1 - D_2)/(D_1 + D_2) = 0.2$ . The blue and orange arrows identify the TE and TM electric field components of the excitations. **c,d)** COMSOL finite-element simulation of (c) the transmittance  $|S_{21}|^2$ , where  $S_{21}$  is the complex transmission coefficient, and (d) of the phase of  $S_{21}$  for the two orthogonal excitations. **e)** Measured transmitted intensity through the metasurface for an impinging beam at normal incidence with the electric field polarized either TE or TM polarization, in blue and orange, respectively.

ing on the device can be conveniently decomposed as  $\mathbf{E} = \mathbf{E}_{\text{TE}} e^{i\delta_{\text{TE}}} + \mathbf{E}_{\text{TM}} e^{i\delta_{\text{TM}}}$ , where  $\mathbf{E}_{\text{TE,TM}}$  are the transverse-electric (TE) and transverse-magnetic (TM) amplitudes, parallel and perpendicular

to the nanowires (i.e., the  $z$  axis, see also Fig. 1b), respectively, and  $\delta_{\text{TE,TM}}$  are the corresponding phases. Therefore, the light polarization is defined by the amplitude and phase relation between these two orthogonal components. The polarization of an arbitrary superposition of TE and TM components – e.g., a linear polarization oriented at  $45^\circ$  with respect to the horizontal axis – can be modified by changing both their relative amplitude and relative phase  $\delta = \delta_{\text{TE}} - \delta_{\text{TM}}$ . In the presented metasurface, this is achieved by exploiting the in-plane birefringence of the  $x$ -cut  $\text{LiNbO}_3$ , which produces a spectral mismatch between TE and TM narrowband resonances. In other words, in a given wavelength interval, only one component of the optical field interacts with the metasurface, undergoing a wavelength-dependent amplitude variation and phase shift  $\Delta\delta(\lambda)$ . The other one, instead, remains unaffected when crossing the sample.

The polarization of the transmitted beam can be subsequently tuned by shifting the central wavelength  $\lambda_0$  of the resonance through the change in the material refractive index induced by an electrical bias. The metasurface has been specifically designed to support a resonance excited by a TE optical field in the telecommunication C-band (i.e., 1530–1565 nm), therefore the biasing field is applied to the metasurface by in-plane gold electrodes positioned  $15\text{ }\mu\text{m}$  apart, perpendicularly to the nanowires. According to numerical simulations<sup>23</sup>, the biasing electric field is approximately uniform within the  $\text{LiNbO}_3$  substrate and aligned parallel to the crystallographic  $z$  axis. In this geometry, the variation of the refractive index for the TE optical field component is determined by the  $r_{33}$  component of the  $\text{LiNbO}_3$  EO tensor, which is the largest one ( $35\text{ pm V}^{-1}$ , see Ref. 33). The applied field modifies the  $\text{LiNbO}_3$  extraordinary index according to the expression<sup>34</sup>

$$\Delta n_e = \frac{1}{2} n_e^3 r_{33} E_z. \quad (1)$$

The narrowband character of the resonance increases the sensitivity to small  $\Delta n_e$  thanks to the sizable spectral shift of the resonance central wavelength  $\lambda_0$  with respect to the resonance linewidth  $\delta\lambda_0$ , that can be obtained even at low bias voltages.

The realized device (see Fig. 1b), whose fabrication process is described elsewhere<sup>23</sup>, consists in a waveguiding  $\text{LiNbO}_3$  thin film atop a  $2\text{ }\mu\text{m}$ -thick  $\text{SiO}_2$  layer, supporting high- $Q$  guided mode resonances arising from the translational symmetry reduction introduced by the patterned periodic nanowires<sup>35,36</sup>. In the case of a sub-wavelength grating characterized by a  $xz$  mirror symmetry, a symmetry-protected bound state in the continuum (BIC) is present for a vanishing in-plane wavevector  $k_{\parallel} = 0$ . As in Ref. 23, to open a radiation channel to this mode at normal incidence, the  $xy$  mirror symmetry is broken by introducing a slight asymmetry in the nanowires dimensions,

turning the BIC into quasi-BIC, with a finite quality-factor. This is achieved by realizing a grating with a subwavelength periodicity of 800 nm, characterized by an asymmetry factor  $\alpha$ , defined as  $\alpha = (D_1 - D_2)/(D_1 + D_2)$ , with  $D_1$  and  $D_2$  equal to the lateral size of the reliefs in each unit cell (see Fig. 1b), equal to 0.2 and filling factor  $FF = 1 - (D_1 + D_2)/p = 0.3$ . According to numerical simulations, the resulting quasi-BIC, excited by TE polarization, emerges at the telecommunication wavelength of  $\lambda_0 \simeq 1547$  nm (see Fig. 1c) with a theoretical quality-factor as high as  $Q = 10^4$ . As evidenced by the numerical simulations in Fig. 1c, the quasi-BIC gives rise to a sharp Fano resonance in the sample transmittance  $|S_{21}|^2$ , together with a steep, abrupt variation of the phase of the transmission coefficient  $S_{21}$  (see Fig. 1d). Conversely, the transmission spectrum of the TM polarization appears featureless.

The sample resonant properties are characterized in a transmission spectroscopy setup with detection unsensitive to the light polarization. The sample is illuminated with a continuous-wave tuneable diode laser in the communication C-band and the transmitted power is collected by a photodiode (see Supplementary Information, S4). Figure 1e shows the transmission spectra obtained as a function of the wavelength of a TE- or TM-polarized beam. The quasi-BIC mode is observed as a pronounced dip in the TE transmission spectrum with an asymmetric profile. The resonance central wavelength  $\lambda_0 \simeq 1553.80$  nm and linewidth  $\delta\lambda_0 = 0.17$  nm are retrieved upon fitting the mode profile with a Fano lineshape<sup>37</sup>. The resulting resonance quality factor  $Q = \lambda_0/\delta\lambda \simeq 9000$  is in agreement with the results reported in Ref. 23. Conversely, the TM optical component doesn't show any sharp feature in the same spectral region. We mention that the raw transmission spectra were affected by strong Fabry-Pérot oscillations compatible with a thickness of the Si substrate of about 400 nm. Therefore, we fitted the original data with the transmissivity of a Fabry-Pérot cavity, removing the corresponding oscillating contribution to obtain the spectra reported in Fig. 1e (see Section S3, Supplementary Information).

### A. Characterization and modulation of the polarization

The rotation and retardation effects imparted by the sample on the light polarization are assessed by evaluating the Stokes parameters of the transmitted radiation for different input polarization states. The light polarization state is conveniently expressed in terms of the Stokes vector  $\mathbf{S} = [S_1 \ S_2 \ S_3,]$  whose components can be determined from light observables<sup>38</sup>. The last three elements represent the degree of polarization projected onto three orthogonal polarization bases. In

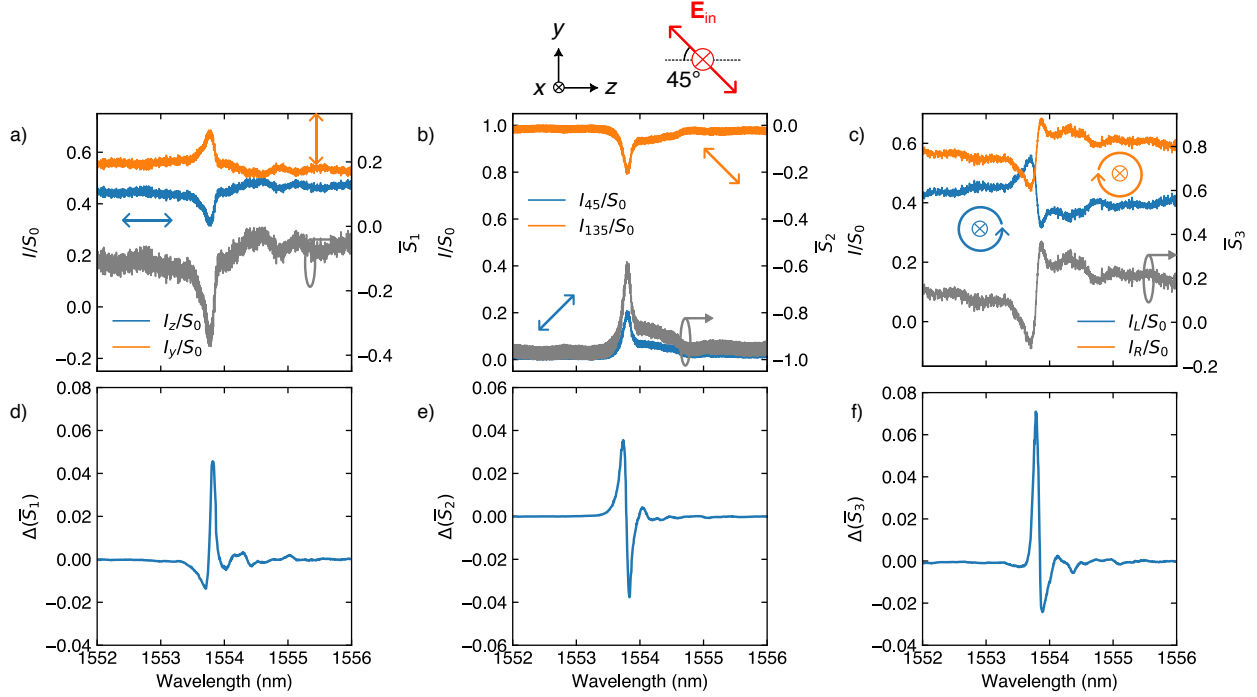


FIG. 2. Across-resonance static and dynamic characterization of the transmitted polarization for an impinging beam linearly polarized at  $135^\circ$  with respect to the  $\text{LiNbO}_3$   $z$  axis (see sketch on top). **a)–c)** Plot of the orthogonal polarization states in blue (orange), in the linear  $z$  ( $y$ ), linear diagonal  $45^\circ$  ( $135^\circ$ ) and circular left (right) basis, respectively. The intensities in each panel are normalized to the total intensity  $S_0 = I_a + I_b$ , where  $I_{a,b}$  are the two measured projections in the corresponding basis. In grey, the corresponding normalized Stokes parameters  $\bar{S}_1$ ,  $\bar{S}_2$  and  $\bar{S}_3$ . **d) – f)** Variation of the normalized Stokes parameters upon application of a sinusoidal driving voltage with peak-to-peak amplitude  $V_{\text{pp}} = 10\text{ V}$  and frequency  $f_{\text{mod}} = 1\text{ MHz}$ .

particular,  $S_1 = |Z\rangle - |Y\rangle$ ,  $S_2 = |D\rangle - |A\rangle$  and  $S_3 = |R\rangle - |L\rangle$ , where  $|\cdot\rangle$  are the intensities projected on the  $z$  or  $y$  axes, on the direction at  $\pm 45^\circ$  with respect to these axes, and on the circular left or right polarization states, respectively. The total intensity is defined as  $S_0 = |a\rangle + |b\rangle$ , where  $|a,b\rangle$  are the two orthogonal projections in a given basis. The transmitted  $S_1$  and  $S_2$  components are determined by means of a polarization analyzer placed before the detector, while for measurements in the circular basis  $S_3$  a broadband quarter-wavelength retarder is introduced before the analyzer. Stokes formalism, at variance with the Jones formalism, is also suitable for the description of depolarization effects. As will be discussed in the following section, to completely describe the device properties with intensity measurements, at least one Stokes vector measurement in each basis set is required<sup>39</sup>. As an example, the case of an antidiagonal input polarization state  $|\text{IN}\rangle = |A\rangle$ ,

with an associated Stokes vector  $\mathbf{S}_{\text{in}} = \begin{bmatrix} 0 & -1 & 0 \end{bmatrix}$ , corresponding to a linearly polarized impinging beam at an angle of  $135^\circ$  with respect to the  $\text{LiNbO}_3$   $z$  axis, will be explicitly discussed. The characterization of other polarizations can be found in Section S1 of the Supplementary Information. Figures. 2a–c) show the normalized intensities projected onto the orthogonal axes for each of the three polarization bases and the corresponding normalized Stokes parameters  $S_i/S_0$ . For simplicity, we will refer to  $\bar{S}_i$  as the normalized Stokes parameters throughout the text. As discussed above, the dispersive birefringence and transmittance of the metasurface, when probed at the TE resonant mode, induces variations of the beam phase and amplitude, respectively. As a consequence, the Stokes parameters exhibit a strong modulation across the resonance profile. In particular, the attenuation of the TE component produces a rotation of the polarization axis toward the  $y$  axis, as shown by the dip in the  $\bar{S}_1$  parameter (see Fig. 2a) and by the corresponding increase of the diagonally-polarized intensity  $I_{45}$  (see Fig. 2b). Moreover, the variable phase shift  $\delta_{\text{TE}}(\lambda)$  results in a change in the  $\bar{S}_3$  parameter, thereby modifying the polarization ellipticity (see Fig. 2c).

The polarization state can be modulated exploiting the EO effect upon the application of an external bias to the electrodes, which modifies the  $\text{LiNbO}_3$  extraordinary index  $n_e$  according to Eq. (1). We perform a dynamic modulation by applying a sinusoidal voltage  $V(t) = \frac{V_{\text{pp}}}{2} \sin(2\pi f_{\text{mod}} t)$ . Under the assumption of a small EO-induced resonant shift, the transmitted power detected by the photodiode can be expressed as  $P(t) = P_{\text{DC}} + P(f_{\text{mod}}) \sin(2\pi f_{\text{mod}} t)$ . The amplitude of the oscillating component,  $P(f_{\text{mod}})$ , is experimentally determined via lock-in detection, following the procedure described in ref. 23. The device exhibited a tuning sensitivity of the resonance central wavelength of  $5.6 \text{ nm V}^{-1}$ , allowing an amplitude modulation efficiency of  $1.5 \times 10^{-2} \text{ V}^{-1}$  in the small bias regime<sup>23</sup> – i.e., for applied  $V_{\text{pp}} < 10 \text{ V}$ . To estimate the EO-induced polarization change, we first evaluate the shifted spectrum  $P_i(\lambda, V = V_{\text{pp}}/2) = P_{i,\text{DC}}(\lambda) + P_i(\lambda, f_{\text{mod}})$  for  $i$  running over the six projections displayed in Fig. 2 a–c. Then, we compute the corresponding normalized Stokes parameters

$$\bar{S}_i(\lambda, V_{\text{pp}}/2) = \frac{P_a(\lambda, V_{\text{pp}}/2) - P_b(\lambda, V_{\text{pp}}/2)}{S_0(\lambda, V_{\text{pp}}/2)}, \quad (2)$$

where  $P_{a,b}$  are the spectra of the two orthogonal polarizations in the considered basis. The retrieved Stokes parameter modulation amplitudes  $\Delta\bar{S}_i(\lambda) = \bar{S}_i(\lambda, V_{\text{pp}}/2) - \bar{S}_i(\lambda, 0)$  for  $V_{\text{pp}} = 10 \text{ V}$  at a modulation frequency of  $f_{\text{mod}} = 1 \text{ MHz}$  are shown in Figs. 2d–f.

To better visualize the effect of the resonance and of the EO-induced modulation on the light polarization, we estimated the parameters defining the polarization ellipse, which are the rotation

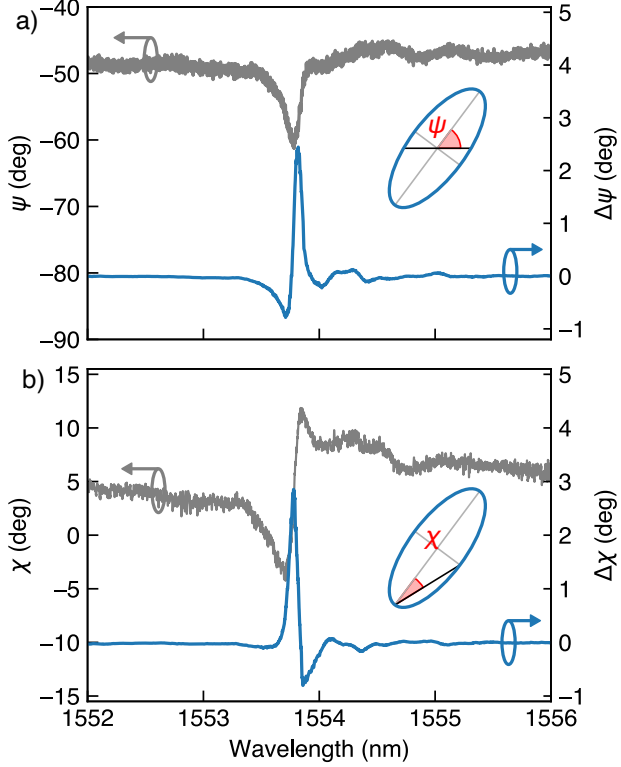


FIG. 3. Dispersion (in grey) and modulation (in blue) of the **a**) ellipse rotation angle  $\psi$  and **b**) of the ellipticity angle  $\chi$  of a  $135^\circ$ -polarized beam, depending on the laser wavelength. The sinusoidal modulating voltage is characterized by  $V_{pp} = 10\text{V}$  and  $f_{\text{mod}} = 1\text{MHz}$ .

angle  $\psi$  and the ellipticity angle  $\chi$  (see the illustrations inside Fig. 3a and b, respectively), which depend on the Stokes parameters according to the following expressions:

$$2\psi = \arctan \frac{\bar{S}_2}{\bar{S}_1}, \quad 2\chi = \arctan \frac{\bar{S}_3}{\sqrt{\bar{S}_1^2 + \bar{S}_2^2}}, \quad (3)$$

while the handedness (or helicity) of the light is determined by the sign of  $\chi$ , with a positive sign standing for RCP light. The dependence of  $\psi$  and  $\chi$  on wavelength is plotted as a grey line in Fig. 3. The maximum rotation  $\Delta\psi$  imparted by the sample is as high as  $15^\circ$ , caused by the attenuation of the  $z$  component of the electric field. A change in ellipticity of  $15^\circ$  is also observed, with a reversal of the helicity when crossing  $\chi = 0$  axis. Concerning the modulation of the polarization ellipse, an absolute change of about  $3^\circ$  is obtained for both the angles for  $V_{pp} = 10\text{V}$  (see Fig. 3 in blue) for wavelengths around  $1553.8\text{ nm}$ .

As a final remark, the frequency response of this sample was characterized in ref. 23, resulting in a modulation bandwidth of  $800\text{ MHz}$ . The same maximum modulation speed is expected also

in this case, since the device time constant was limited by the electrodes capacitance.

## B. Evaluation of the metasurface Mueller matrix

The investigated device modulates the light polarization by inducing amplitude and phase variations in the TE electric field when the metasurface is excited at resonance (see Fig. 1). We now discuss how the phase information can be retrieved from the polarization measurement discussed in the previous section.

The four Stokes parameters are obtained by measuring light intensities, eventually losing the information about the phase. Therefore, the characterization of a single Stokes vector is not sufficient to retrieve this information. To circumvent this problem, we determine the  $4 \times 4$  Mueller matrix  $\mathbf{M}$ , which relates the input and output vectors  $[S_0 \ S_1 \ S_2 \ S_3]$  and fully describes the effect of the device on the light polarization. Here, we note that the total intensity  $S_0$  has been averaged over its definitions in the three orthogonal polarization bases. In the general case,  $\mathbf{M}$  contains 16 independent elements; therefore, determining the Mueller matrix requires a set of at least four independent measurements of the Stokes vector for different input polarization conditions, chosen in such a way that they form a complete basis spanning the Poincaré sphere<sup>39</sup>. As an example, we consider  $\tilde{\mathbf{S}}_{\text{out}(in)} = [\mathbf{S}_{\text{TE}} \ \mathbf{S}_{45} \ \mathbf{S}_{135} \ \mathbf{S}_{\text{L}}]_{\text{out}(in)}$ , that is a  $4 \times 4$  matrix obtained by appending the Stokes column vectors of four different polarization states of the outgoing (incoming) beam analyzed in this manuscript. The total Mueller matrix of the samples is then determined as

$$\mathbf{M} = \tilde{\mathbf{S}}_{\text{out}} \tilde{\mathbf{S}}_{\text{in}}^{-1}. \quad (4)$$

We should recall that the metasurface is not simply dephasing  $\mathbf{E}_{\text{TE}}$  and  $\mathbf{E}_{\text{TM}}$  but is also strongly attenuating the transmitted  $\mathbf{E}_{\text{TE}}$  when illuminated at resonance with the quasi-BIC. Therefore,  $\mathbf{M}$  does not describe a simple phase retarder as it would be for a flat transmission spectrum, and it should be decomposed to disentangle the changes in phase and amplitude of the TE component. We exploit an extensively used approach for Mueller matrix decomposition, consisting in a polar decomposition algorithm developed by Lu and Chipman<sup>40</sup>, which allows writing an arbitrary Mueller matrix as

$$\mathbf{M} = \mathbf{M}_{\Delta} \mathbf{M}_r \mathbf{M}_d, \quad (5)$$

where the three matrices  $\mathbf{M}_{\Delta}$ ,  $\mathbf{M}_r$  and  $\mathbf{M}_d$  account for depolarization (i.e., polarization scrambling), retardation (i.e., change in the relative phase) and diattenuation (i.e., change in the relative ampli-

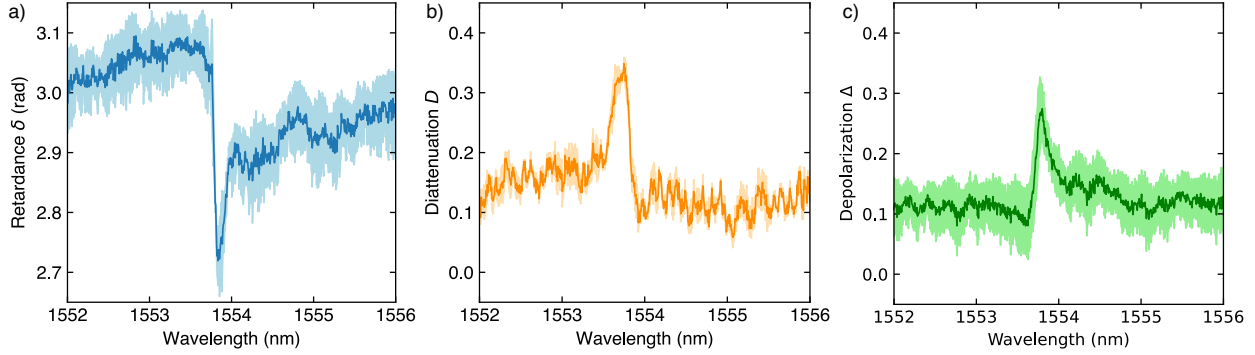


FIG. 4. Spectra of **a** the retardance  $\delta$ , **b** the diattenuation magnitude  $D$  and **c** the depolarization magnitude  $\Delta$ . The solid lines correspond to the average values obtained by calculating the Mueller matrices from four different polarization combinations, while the shaded areas are the corresponding standard deviations.

tude) properties, respectively. Relevant details on the decomposition algorithm are discussed in Section S2 of the Supplementary Information. Three meaningful quantities describing the action of the device on light polarization can be retrieved from the three matrices of Eq. (5):

$$\delta = \cos^{-1} \left( \frac{\text{Tr}\{\mathbf{M}_r\}}{2} - 1 \right), \quad (6a)$$

$$D = \frac{1}{m_{00}} \sqrt{\sum_{j=1}^3 m_{0j}^2}, \quad (6b)$$

$$\Delta = 1 - \frac{1}{3} |\text{Tr}\{\mathbf{M}_\Delta\} - 1|, \quad (6c)$$

where  $\delta = \delta_{\text{TE}} - \delta_{\text{TM}}$  is the applied phase retardation,  $D$  is the diattenuation magnitude, defined by the first row elements of  $\mathbf{M}$ ,  $m_{0,j}$ , and  $\Delta$  is the depolarization magnitude. Thanks to the redundant set of polarization states that we acquired, the quantities defined in Eq. (6) have been determined by averaging the decomposition results obtained from four independently measured Mueller matrices. Their dispersion across the resonance is plotted in Fig. 4. The metasurface modifies the relative phase delay  $\delta$  between the TE and TM components by about  $-0.4$  rad across the resonance (see Fig. 4a), with a dispersion profile that qualitatively reproduces the one displayed in Fig. 1d. It is worth noting that, while the abrupt phase change is preserved, the absolute variation across the resonance is reduced with respect to Fig. 1d. This effect can be ascribed to the ion etching process<sup>41</sup>, which is known to introduce optical losses into the refractive index<sup>42</sup>. Fig. 4b depicts the diattenuation magnitude  $D$ , which is enhanced by the attenuation of  $\mathbf{E}_{\text{TE}}$  upon interaction with the metasurface resonance – the element  $m_{01}/m_{00}$  shows a sharp dip on resonance,

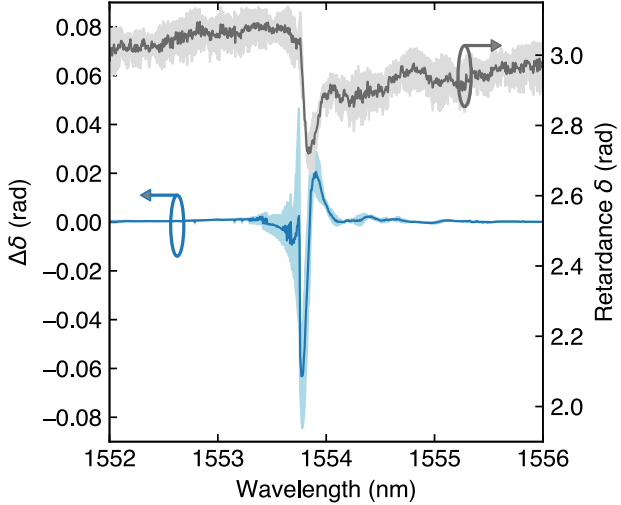


FIG. 5. Wavelength dependence of the retardance  $\delta = \delta_{\text{TE}} - \delta_{\text{TM}}$  (in gray) and of its variation  $\Delta\delta = \delta(V_{\text{pp}}/2) - \delta(0)$  (in blue) upon application of a sinusoidal driving voltage with peak-to-peak amplitude  $V_{\text{pp}} = 10\text{ V}$  and frequency  $f_{\text{mod}} = 1\text{ MHz}$ . The difference  $\Delta\delta$  has been calculated by evaluating  $\delta$  from the metasurface Mueller matrices at 0 V and  $V_{\text{pp}}/2$ . The solid lines are obtained by averaging the results of the decomposition algorithm applied to four different polarization combinations. The shaded areas are the corresponding standard deviations.

see Fig. S3b of the Supplementary Information. Finally, Fig. 4c evaluates the depolarization, that is also increased on resonance. We ascribe this effect to an enhancement of the polarization scrambling introduced by scattering from defects and surface roughness, which are byproducts of the polishing treatment of sample back surface.

Eventually, we evaluate the capability of the device to modulate the relative phase between the TE and TM electric field components by determining the change in the retardance actuated by the applied electric field. Figure 5 shows the amplitude of the retardance modulation  $\Delta\delta = \delta(\lambda, V_{\text{pp}}/2) - \delta(\lambda, 0)$  obtained by applying a sinusoidal bias with  $V_{\text{pp}} = 10\text{ V}$ . The absolute phase variation reaches approximately 0.06 rad, which is in agreement with the measured change in ellipticity of Fig. 3b. Notably, the same phase modulation would require a propagation length around 1 mm assuming a refractive index modulation  $\Delta n = 10^{-4} \div 10^{-5}$  in a non-resonant device.

### III. CONCLUSIONS

In the present work we provided a first experimental demonstration of a LiNbO<sub>3</sub> metasurface for the electro-optical modulation of light polarization. A narrowband quasi-BIC resonance, selectively excited by one specific polarization, induces a sizable attenuation of that component and a corresponding phase variation, which result in polarization rotation and conversion. These effects were quantified by measuring the four Stokes parameters of the transmitted light for different wavelengths and impinging polarization states. The polarization was subsequently modulated by applying a sinusoidal bias, resulting in an absolute variation of the Stokes parameters of the order of 0.05 for a peak-to-poeak bias amplitude  $V_{\text{pp}} = 10\text{V}$  at a modulation frequency of 1 MHz. These changes translated into a variation in the rotation angle and ellipticity of the polarization ellipse of about 3°, corresponding to a sensitivity of 0.6°V<sup>-1</sup>. Eventually, from the measured Stokes parameters the phase variation of the TE-polarized electric field was estimated to be 50 mrad for  $V_{\text{pp}} = 10\text{V}$ . The achieved phase modulation extends the functionalities of nanoscale EO modulators from amplitude to phase and polarization modulation, demonstrating the crucial role of high- $Q$  resonances in enhancing light-matter interaction in sub-wavelength optical devices.

## REFERENCES

<sup>1</sup>S. A. Schulz, R. F. Oulton, M. Kenney, A. Alù, I. Staude, A. Bashiri, Z. Fedorova, R. Kolkowski, A. F. Koenderink, X. Xiao, J. Yang, W. J. Peveler, A. W. Clark, G. Perrakis, A. C. Tasolamprou, M. Kafesaki, A. Zaleska, W. Dickson, D. Richards, A. Zayats, H. Ren, Y. Kivshar, S. Maier, X. Chen, M. A. Ansari, Y. Gan, A. Alexeev, T. F. Krauss, A. Di Falco, S. D. Gennaro, T. Santiago-Cruz, I. Brener, M. V. Chekhova, R.-M. Ma, V. V. Vogler-Neuling, H. C. Weigand, U.-L. Talts, I. Occhiodori, R. Grange, M. Rahmani, L. Xu, S. M. Kamali, E. Arababi, A. Faraon, A. C. Harwood, S. Vezzoli, R. Sapienza, P. Lalanne, A. Dmitriev, C. Rockstuhl, A. Sprafke, K. Vynck, J. Upham, M. Z. Alam, I. De Leon, R. W. Boyd, W. J. Padilla, J. M. Malof, A. Jana, Z. Yang, R. Colom, Q. Song, P. Genevet, K. Achouri, A. B. Evlyukhin, U. Lemmer, and I. Fernandez-Corbaton, “Roadmap on photonic metasurfaces,” **124**, 10.1063/5.0204694.

<sup>2</sup>A. C. Overvig, S. Shrestha, S. C. Malek, M. Lu, A. Stein, C. Zheng, and N. Yu, “Dielectric metasurfaces for complete and independent control of the optical amplitude and phase,” **8**, 92.

<sup>3</sup>H. Wang, Z. Hu, J. Deng, X. Zhang, J. Chen, K. Li, and G. Li, “All-optical ultrafast polarization switching with nonlinear plasmonic metasurfaces,” **10**, eadk3882 () .

<sup>4</sup>F.-J. Li, S. Wang, R. Zhong, M.-X. Hu, Y. Jiang, M. Zheng, M. Wang, X. Li, R. Peng, and Z.-L. Deng, “Metasurface polarization optics: From classical to quantum,” **11**, 041332.

<sup>5</sup>A. Arbabi, Y. Horie, M. Bagheri, and A. Faraon, “Dielectric metasurfaces for complete control of phase and polarization with subwavelength spatial resolution and high transmission,” **10**, 937–943.

<sup>6</sup>M. Khorasaninejad, W. T. Chen, R. C. Devlin, J. Oh, A. Y. Zhu, and F. Capasso, “Metalenses at visible wavelengths: Diffraction-limited focusing and subwavelength resolution imaging,” **352**, 1190–1194.

<sup>7</sup>N. A. Rubin, G. D’Aversa, P. Chevalier, Z. Shi, W. T. Chen, and F. Capasso, “Matrix fourier optics enables a compact full-stokes polarization camera,” **365**, eaax1839.

<sup>8</sup>Y. Luan, A. Zilli, A. Di Francescantonio, V. Vinel, P. Biagioni, L. Duò, A. Lemaître, G. Leo, M. Celebrano, and M. Finazzi, “All-optical polarization encoding and modulation by nonlinear interferometry at the nanoscale,” **14**, 318.

<sup>9</sup>J. Ma, J. Zhang, Y. Jiang, T. Fan, M. Parry, D. N. Neshev, and A. A. Sukhorukov, “Polarization engineering of entangled photons from a lithium niobate nonlinear metasurface,” **23**, 8091–8098.

<sup>10</sup>O. A. M. Abdelraouf, Z. Wang, H. Liu, Z. Dong, Q. Wang, M. Ye, X. R. Wang, Q. J. Wang, and H. Liu, “Recent advances in tunable metasurfaces: Materials, design, and applications,” **16**, 13339–13369.

<sup>11</sup>G. P. Zograf, M. I. Petrov, S. V. Makarov, and Y. S. Kivshar, “All-dielectric thermonanophotonics,” **13**, 643.

<sup>12</sup>C. Jung, E. Lee, and J. Rho, “The rise of electrically tunable metasurfaces,” **10**, eado8964.

<sup>13</sup>M. Maiuri, A. Schirato, G. Cerullo, and G. Della Valle, “Ultrafast all-optical metasurfaces: Challenges and new frontiers,” **11**, 2888–2905.

<sup>14</sup>C. Wang, M. Zhang, X. Chen, M. Bertrand, A. Shams-Ansari, S. Chandrasekhar, P. Winzer, and M. Lončar, “Integrated lithium niobate electro-optic modulators operating at CMOS-compatible voltages,” **562**, 101–104 ()�.

<sup>15</sup>K. Koshelev, Y. Tang, K. Li, D.-Y. Choi, G. Li, and Y. Kivshar, “Nonlinear metasurfaces governed by bound states in the continuum,” **6**, 1639–1644, publisher: American Chemical Society (ACS).

<sup>16</sup>M. Zhang, C. Wang, R. Cheng, A. Shams-Ansari, and M. Lončar, “Monolithic ultra-high-q lithium niobate microring resonator,” **4**, 1536 ()�.

<sup>17</sup>Y. Akahane, T. Asano, B.-S. Song, and S. Noda, “High-q photonic nanocavity in a two-dimensional photonic crystal,” **425**, 944–947.

<sup>18</sup>D. Sanvitto, A. Daraei, A. Tahraoui, M. Hopkinson, P. W. Fry, D. M. Whittaker, and M. S. Skolnick, “Observation of ultrahigh quality factor in a semiconductor microcavity,” **86**, 191109.

<sup>19</sup>A. Weiss, C. Frydendahl, J. Bar-David, R. Zektzer, E. Edrei, J. Engelberg, N. Mazurski, B. Desiatov, and U. Levy, “Tunable metasurface using thin-film lithium niobate in the telecom regime,” **9**, 605–612, publisher: American Chemical Society (ACS).

<sup>20</sup>C. Damgaard-Carstensen and S. I. Bozhevolnyi, “Nonlocal electro-optic metasurfaces for free-space light modulation,” **12**, 2953–2962.

<sup>21</sup>J. Zhang, Y. Kosugi, M. Ogasawara, K. Ariu, A. Otomo, T. Yamada, Y. Nakano, and T. Tanemura, “High-speed metasurface modulator using perfectly absorptive bimodal plasmonic resonance,” **8** (), 10.1063/5.0173216.

<sup>22</sup>C. Damgaard-Carstensen, T. Yezekyan, M. L. Brongersma, and S. I. Bozhevolnyi, “Highly efficient, tunable, electro-optic, reflective metasurfaces based on quasi-bound states in the continuum,” **19**, 11999–12006.

<sup>23</sup>A. Di Francescantonio, A. Sabatti, H. Weigand, E. Baily-Rioufreyt, M. A. Vincenti, L. Carletti, J. Kellner, A. Zilli, M. Finazzi, M. Celebrano, and R. Grange, “Efficient GHz electro-optical modulation with a nonlocal lithium niobate metasurface in the linear and nonlinear regime,” **16**, 7000.

<sup>24</sup>S. Dagli, J. Shim, H. Carr Delgado, H. B. Balch, S. Abdollahramezani, C. Chen, V. Dolia, E. Klopfer, J. Dixon, J. Hu, B. Ogunlade, J. Song, M. L. Brongersma, D. Barton, and J. A. Dionne, “GHz-speed wavefront shaping metasurface modulators enabled by resonant electro-optic nanoantennas,” **37**, e06790.

<sup>25</sup>I.-C. Benea-Chelmu, S. Mason, M. L. Meretska, D. L. Elder, D. Kazakov, A. Shams-Ansari, L. R. Dalton, and F. Capasso, “Gigahertz free-space electro-optic modulators based on mie resonances,” **13**, 10.1038/s41467-022-30451-z, publisher: Springer Science and Business Media LLC.

<sup>26</sup>G. Soma, K. Ariu, S. Karakida, Y. Tsubai, and T. Tanemura, “Subvolt high-speed free-space modulator with electro-optic metasurface,” 10.1038/s41565-025-02000-4.

<sup>27</sup>L. Wang, F. Setzpfandt, and I. Shadrivov, “Tunable anisotropic electro-optic metasurfaces,” **13**, 3376.

<sup>28</sup>Y. Hou, Y. Xu, B. Du, Y. Zhang, and L. Zhang, “Electrically tunable dual polarization states of light using lithium niobate-based nanograting,” **49**, 470.

<sup>29</sup>F. Ding, C. Meng, and S. I. Bozhevolnyi, “Electrically tunable optical metasurfaces,” **3**, R07.

<sup>30</sup>P. Yu, J. Li, and N. Liu, “Electrically tunable optical metasurfaces for dynamic polarization conversion,” **21**, 6690–6695.

<sup>31</sup>M. Zhang, W. Zhang, A. Q. Liu, F. C. Li, and C. F. Lan, “Tunable polarization conversion and rotation based on a reconfigurable metasurface,” **7**, 12068 () .

<sup>32</sup>M. Bosch, M. R. Shcherbakov, Z. Fan, and G. Shvets, “Polarization states synthesizer based on a thermo-optic dielectric metasurface,” **126**, 073102.

<sup>33</sup>R. J. Holmes, Y. S. Kim, C. D. Brandle, and D. M. Smyth, “Evaluation of crystals of LiNbO<sub>3</sub> doped with MgO or TiO<sub>2</sub> for electrooptic devices,” **51**, 41–45.

<sup>34</sup>A. Fedotova, L. Carletti, A. Zilli, F. Setzpfandt, I. Staude, A. Toma, M. Finazzi, C. De Angelis, T. Pertsch, D. N. Neshev, and M. Celebrano, “Lithium niobate meta-optics,” **9**, 3745–3763, publisher: American Chemical Society (ACS).

<sup>35</sup>L. Huang, R. Jin, C. Zhou, G. Li, L. Xu, A. Overvig, F. Deng, X. Chen, W. Lu, A. Alù, and A. E. Miroshnichenko, “Ultrahigh-q guided mode resonances in an all-dielectric metasurface,”

**14**, 10.1038/s41467-023-39227-5, publisher: Springer Science and Business Media LLC.

<sup>36</sup>K. Sun, H. Wei, W. Chen, Y. Chen, Y. Cai, C.-W. Qiu, and Z. Han, “Infinite-q guided modes radiate in the continuum,” **107**, 115415–115415.

<sup>37</sup>M. F. Limonov, “Fano resonance for applications,” **13**, 703–703.

<sup>38</sup>E. Hecht, *Optics*, 5th ed. (Pearson Education, Inc).

<sup>39</sup>S. G. Reddy, S. Prabhakar, A. Aadhi, A. Kumar, M. Shah, R. P. Singh, and R. Simon, “Measuring the mueller matrix of an arbitrary optical element with a universal SU(2) polarization gadget,” **31**, 610.

<sup>40</sup>S.-Y. Lu and R. A. Chipman, “Interpretation of mueller matrices based on polar decomposition,” **13**, 1106.

<sup>41</sup>B. Gao, M. Ren, W. Wu, W. Cai, and J. Xu, “Electro-optic lithium niobate metasurfaces,” **64**, 10.1007/s11433-021-1668-y, publisher: Springer Science and Business Media LLC.

<sup>42</sup>R. Geiss, S. Dizian, M. Steinert, F. Schrempel, E. Kley, A. Tünnermann, and T. Pertsch, “Photonic crystals in lithium niobate by combining focussed ion beam writing and ion-beam enhanced etching,” **211**, 2421–2425.